small
NANO MICRO
www.small-journal.com

Graphene Scroll-Coated α-MnO_2 Nanowires as High-Performance Cathode Materials for Aqueous Zn-Ion Battery

Buke Wu, Guobin Zhang, Mengyu Yan, Tengfei Xiong, Pan He, Liang He, Xu Xu, and Liqiang Mai**

The development of manganese dioxide as the cathode for aqueous Zn-ion battery (ZIB) is limited by the rapid capacity fading and material dissolution. Here, a highly reversible aqueous ZIB using graphene scroll-coated α-MnO_2 as the cathode is proposed. The graphene scroll is uniformly coated on the MnO_2 nanowire with an average width of 5 nm, which increases the electrical conductivity of the MnO_2 nanowire and relieves the dissolution of the cathode material during cycling. An energy density of 406.6 Wh kg^{-1} (382.2 mA h g^{-1}) at 0.3 A g^{-1} can be reached, which is the highest specific energy value among all the cathode materials for aqueous Zn-ion battery so far, and good long-term cycling stability with 94% capacity retention after 3000 cycles at 3 A g^{-1} are achieved. Meanwhile, a two-step intercalation mechanism that Zn ions first insert into the layers and then the tunnels of MnO_2 framework is proved by in situ X-ray diffraction, galvanostatic intermittent titration technique, and X-ray photoelectron spectroscopy characterizations. The graphene scroll-coated metallic oxide strategy can also bring intensive interests for other energy storage systems.

1. Introduction

With the outbreak of the industrial revolution nowadays, the energy industry is facing unprecedented challenges of developing high-performance energy storage system with long life, low cost, and environmental friendliness demanded by the human society.[1] Throughout the entire energy storage technologies, lithium ion batteries have dominated the global energy storage market for a long time due to their high energy density and long cycling life. However, the potential safety problems, pollution concerns, high cost, and limited lithium resources are still the critical challenges.[2] Recently, aqueous Zn-ion battery (ZIB) becomes a hot research area. On the one hand, Zn metal has a remarkable theoretical capacity (819 mA h g^{-1}) and is easy to obtain, transport, and store.[3] On the other hand, compared with organic electrolytes, aqueous electrolytes are much safer and cheaper.[4] Despite many merits of ZIB, it is still difficult to find proper cathode material as the host for storage of Zn ions. Previous studies focused on the Prussian blue, but it delivered a relatively low capacity of 50 mA h g^{-1}.[5] Vanadium-based materials, such as V_2O_5,[6] $Zn_{0.25}V_2O_5$,[7] and VS_2,[8] are another series of potential candidates as cathode material for aqueous ZIB due to their considerable capacity and good cycling stability, but still limited by low operating voltage.

Manganese dioxide shows both decent theoretical capacity and considerable theoretical voltage versus Zn, but its development is hindered by the rapid capacity fading, caused by the dissolution of MnO_2 in the electrolyte, as well as the irreversible byproducts.[9] Alkaline electrolytes and mild electrolytes containing Zn^{2+} are commonly used in Zn/MnO_2 cells.[10] Recently Liu and co-workers presented an aqueous electrolyte with $MnSO_4$ additive which could prevent the dissolution of Mn^{2+} from Mn^{3+} disproportion and reduce the accumulation of the byproducts from both cathode and anode. As a result, the cycling performance of the aqueous Zn/MnO_2 battery was greatly improved.[11]

Some other methods are also applied to improve the electrochemical performances of aqueous Zn/MnO_2 battery. For example, carbon-based materials, especially graphene, are widely used to improve the electrical conductivity of MnO_2 cathode materials.[12] For instance, Hu et al. successfully assembled single nanowire device based on MnO_2 and reduced graphene oxide (rGO), and the electrical conductivity of MnO_2 nanowire (MNW) was greatly improved.[12b] But the reaction mechanism of MnO_2 cathode and Zn anode is still unclear. Some researchers demonstrated that the insertion products like $Zn_xMn_2O_4$,[13] $ZnMn_2O_4$,[10a] and Zn-buserite formed by insertion/extraction of Zn ions into/from MnO_2 framework.[14] However, the conversion reaction between MnO_2 and MnOOH was also discussed in recent studies. So, a more comprehensive reaction mechanism remains to be revealed in this system.[11]

B. Wu, G. Zhang, Dr. M. Yan, T. Xiong, P. He, Prof. L. He, Dr. X. Xu, Prof. L. Mai
State Key Laboratory of Advanced Technology for Materials Synthesis and Processing
International School of Materials Science and Engineering
Wuhan University of Technology
Wuhan 430070, P. R. China
E-mail: ymymiles@whut.edu.cn; mlq518@whut.edu.cn
Dr. M. Yan
Materials Science and Engineering Department
University of Washington
Seattle, WA 98195-2120, USA
Prof. L. He
Department of Materials Science and NanoEngineering
Rice University
Houston, TX 77005, USA
The ORCID identification number(s) for the author(s) of this article can be found under https://doi.org/10.1002/smll.201703850.

DOI: 10.1002/smll.201703850

Herein, we demonstrate a highly reversible aqueous ZIB using α-MnO_2/graphene scrolls (MGS) as the cathode material. The rGO scrolls reduce the dissolution of the MnO_2 during cycling. The cathode delivers a prominent capacity (362.2 mA h g^{-1} at a current density of 0.3 A g^{-1}), long-term cyclability (87.4 mA h g^{-1} after 800 cycles at an extremely high current density of 7 A g^{-1}, 145.3 mA h g^{-1} at 3 A g^{-1}), and superior rate capability compared with bare MNW. Moreover, the electrochemical reaction mechanism of MGS electrode is further investigated and a two-step intercalation mechanism is elucidated and proved by in situ X-ray diffraction (XRD), galvanostatic intermittent titration technique (GITT), and X-ray photoelectron spectroscopy (XPS) characterizations.

2. Results and Discussion

The schematic of synthesis process of MGS is shown in **Figure 1**. Briefly, $MnSO_4 \cdot H_2O$ and $KMnO_4$ were dissolved in deionized (DI) water to obtain the manganese oxide precursor with uniform grain size. Reduced graphene oxide suspension was then added, and after ultrasonication and stirring, the manganese oxide precursor was attached to the surface of rGO sheets by the hydrogen bonds between MnO_6 octahedrons and functional groups on the surface of rGO sheets.[15] Then the suspension was sealed into a Teflon-lined autoclave for hydrothermal reaction. According to previous study,[16] the pH value is an important issue in controlling the phase of the MnO_2. When the pH value of reaction solution changed to 2, the MnO_4^- oxidation ability is increased in the acidic condition, and the K^+ becomes the support of the 2×2 tunnel structure, because of the large size of K^+ cation with the effective hydrated radius of 137 pm, which leads to the creation of α-MnO_2 successfully. From scanning electron microscopy (SEM) images of the samples from different hydrothermal time, the particles gradually grow into nanowires with rGO sheets coating, then MGS forms after hydrothermal reaction for 12 h.

The crystal structures of the prepared MNW and MGS were characterized by XRD (**Figure 2**a). All characteristic peaks match well with the standard card of α-MnO_2 (JCPDS No. 44-0141). The Raman spectra of MNW and MGS in the range of 400–800 cm^{-1} are shown in Figure S1 (Supporting Information). The peaks located at 564 and 644 cm^{-1} are observed, corresponding to stretching modes of MnO_6 octahedrons.[17] The SEM and transmission electron microscope (TEM) images (Figure 2b,d) show the uniform morphology of MGS with a diameter ranging from 50 to 200 nm and length up to 0.5–3 µm. TEM/energy-dispersive X-ray spectroscopy (EDS) line scan (Figure 2c) result further confirms the coating of rGO. Mn and O elements are mostly distributed in the center of nanowire, while C element is distributed on the edge of the nanowire. From the thermogravimentric (TG) results in Figure S2 (Supporting Information), we figure out that the total carbon content in MGS is 3.6%. From the edge of nanowire (Figure 2e), we can find that the thicker nanowire is actually aggregated by several single nanowires. On the edge of MGS, multilayer rGO with thickness of 5 nm is clearly observed (Figure 2f), and the lattice spacings of 0.23 and 0.48 nm are found to match well with (330) and (200) crystal planes of α-MnO_2, respectively.

In order to investigate the electrochemical performance of the MGS, CR2016 coin-type cells were assembled, and 2 M $ZnSO_4$ and 0.2 M $MnSO_4$ mixture solution was chosen as the electrolyte. Figure S3a (Supporting Information) shows the capacities of MNW and MGS with different content of rGO additive (weight percentages of 0.9%, 1.8%, 2.7%, and 3.6%) at the current density of 0.3 A g^{-1} within the voltage range of 1.00–1.85 V. The capacity increases significantly with the increasing content of rGO and remains almost unchanged for MGS-3.6% (with rGO content of 3.6%). The result shows that rGO can vastly improve the capacity of MNW as the cathode material of aqueous ZIB, and the optimum rGO content is 3.6%. Therefore, in this work, MGS with 3.6% graphene additive (MGS-3.6%) was chosen as the experimental group, and the MNW was chosen for comparison. Figure S3b (Supporting Information) shows the cyclic voltammogram (CV) curves of MNW and MGS. The CV curve of MNW has two pairs of reduction/oxidation peaks located at 1.27/1.39 and 1.55/1.60 V, and MGS's peaks located at 1.25/1.38 and 1.55/1.61 V, indicating a similar redox behavior. Therefore, the rGO coating does not significantly influence the mechanism of redox reactions in α-MnO_2 cathode. Except adding Mn^{2+} into the electrolyte to inhibit dissolution of Mn^{2+} from Mn^{3+} disproportionation into the electrolyte during cycling, we believe that rGO is another effective strategy to improve the stability of MnO_2 as the cathode material. This is confirmed by an inductively coupled plasma (ICP) analysis of the Mn and Zn element concentration in a 2 M $ZnSO_4$ electrolyte solution (**Figure 3**a). The concentration of the dissolved Mn element decreases during the discharge process after the rGO coating, which proves that MGS is more stable than MNW as the cathode for aqueous ZIB. The Nyquist plots (Figure S4, Supporting Information) demonstrate that rGO improves the charge transfer kinetics of MnO_2 as the cathode material for aqueous ZIB. The fitting result shows that the charge transfer resistance (R_{ct}) of MGS (175.6 Ω) is lower than that of MNW (355.5 Ω) before cycling. Meanwhile, in terms of the rate performance, MGS cathode delivers the capacities of 301.2, 282.6, 250.2, 226.6, and 165.7 mA h g^{-1} at discharge–charge rate of 0.1, 0.3, 0.5, 1.0, and 3.0 A g^{-1}, respectively, while MNW delivers the capacities of 242.3, 176.4, 151.5, 104.3, and 58.9 mA h g^{-1} at the same current densities (Figure 3b). MGS also shows a high reversibility in aspect of cycling performance. After activation at a current density of 0.1 A g^{-1} for ten cycles, the capacity can reach 382.2 mA h g^{-1} (406.6 Wh kg^{-1}) at 0.3 A g^{-1}, which is the highest specific energy value among all the cathode materials for aqueous Zn-ion battery so far, and remains 362.6 mA h g^{-1} after 100 cycles with capacity retention of 95%. At 1.0 A g^{-1}, the capacity can still achieve 239.8 mA h g^{-1} after 100 cycles (Figure 3c). Long-term cycling performance is also an important parameter for batteries. At an extremely high current density of 7 A g^{-1} (Figure 3d), MGS also shows good stability and considerable capacity which remains 87.4 mA h g^{-1} after 800 cycles. Furthermore, at a lower current density of 3 A g^{-1} (inset of Figure 3d), MGS cathode shows an excellent capacity of 145.3 mA h g^{-1} with a high capacity retention of 94% after 3000 cycles. Figure 3e shows the charge and discharge curves of MGS at various current densities. The discharge curve is divided into two platforms with the turning point at 1.30 V. The capacities from the discharge platform I (DP I,

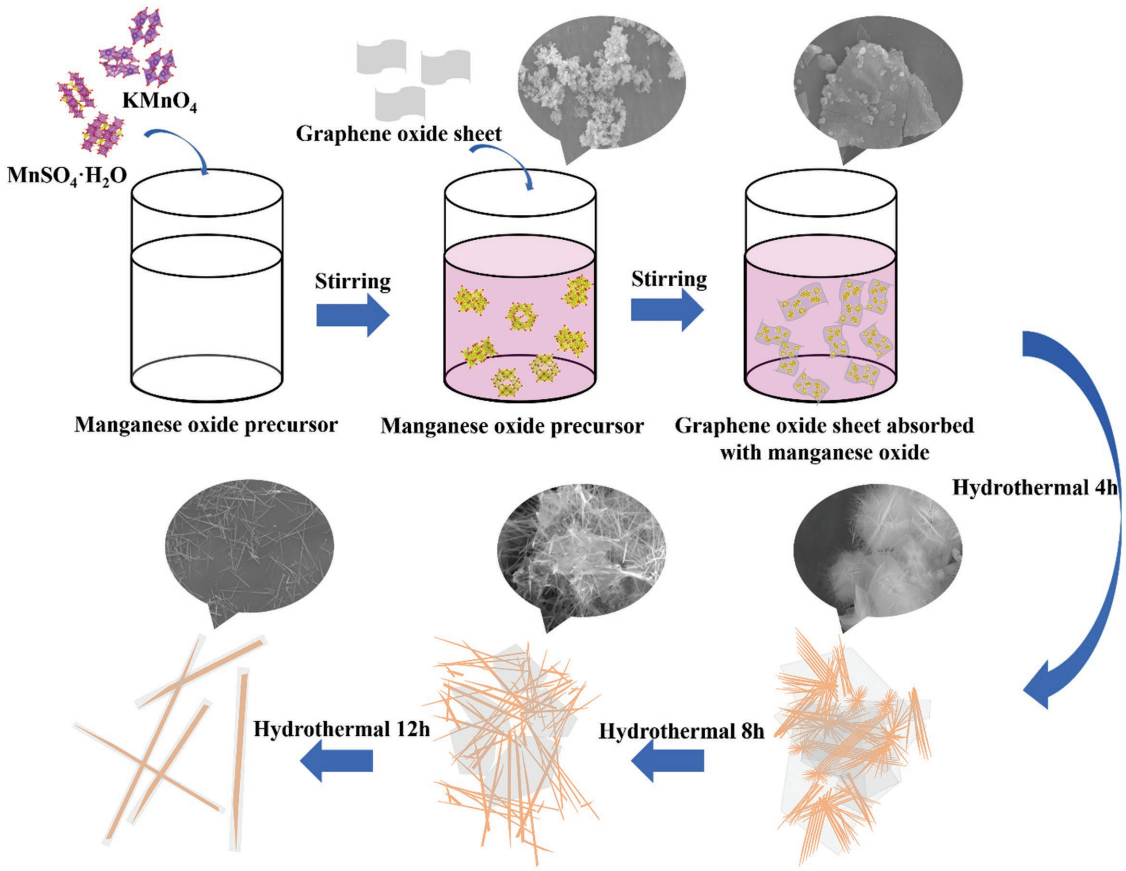

Figure 1. Schematic illustration of the formation of the MGS.

within the voltage range of 1.30–1.85 V) and discharge platform II (DP II, within the voltage range of 1.00–1.30 V) are calculated separately in Figure S5b (Supporting Information). With rGO coating, the capacity of DP I does not decreases dramatically as the current density increases, which is 146.4, 150.5, 147.1, 147.0, and 126.1 mA h g^{-1} at 0.1, 0.3, 0.5, 1.0, and 3.0 A g^{-1}, respectively. While those of MNW decrease sharply at the same current densities, which are 151.7, 121.3, 110.2, 76.2, and 48.2 mA h g^{-1}, respectively (Figure S5a, Supporting Information). Besides, both capacities of DP II of MGS and MNW decrease more evidently than those of DP I as the current density increases. Ragone plots (specific energy vs specific power) by comparing the Zn/MGS system to reported α-MnO_2,[11] Todorokite-typy MnO_2,[18] β-MnO_2,[14b] VS_2,[8] and $Zn_{0.25}V_2O_5$[7] cathodes for aqueous ZIBs (Figure 3f; Table S1, Supporting Information). High specific energy and specific power (406.6 Wh kg^{-1} at 135W kg^{-1}; 381.5 Wh kg^{-1} at 405 W kg^{-1}; 338.1 Wh kg^{-1} at 675 W kg^{-1}; 305.9 Wh kg^{-1} at 1350 W kg^{-1}; 223.7 Wh kg^{-1} at 4050 W kg^{-1}, and 109.2 Wh kg^{-1} at 9450 W kg^{-1}) can be simultaneously achieved, which is promising for energy storage applications.

In Figure 3c,d, the discharge capacities increase gradually during the activation process of first 10 cycles. We attribute this capacity increase to the gradual activation of electrodes. It has three meanings here. First, it means that the electrolyte gradually soaks the cathode material, which is a common phenomenon for all aqueous battery. Second, based on the very recent study,[14b] Chen group used X-ray absorption spectroscopy and X-ray near edge absorption structure to reveal the tunnel-structured manganese dioxide polymorphs undergo a phase transition to layered zinc-buserite during first discharging which allows subsequent intercalation of zinc cations into the latter structure. This explains why the first charge–discharge curve has only one discharge platform, unlike the later curve with two platforms. Last but not the least, to alleviate the dissolution of Mn^{2+} from Mn^{3+} disproportion and reduce the accumulation of the byproducts from both cathode and anode, $MnSO_4$ is added into the electrolyte.[11] Under high voltage up to 1.85 V, the Mn^{2+} can be deposited on the surface of the cathode material, which causes the gradual increasing of the capacity during the first few cycles. The time of this process depends on the current density of the testing, and higher current density takes more time to reach the highest specific capacity than lower current density does.[14b] To confirm this oppinion, rGO was used as the cathode material versus Zn anode in a 2M $ZnSO_4$ and 0.2 M $MnSO_4$ mixture electrolyte to prove the reverdible deposition of Mn^{2+} in electrolyte. The cycling performance of Zn/rGO cell is shown in Figure S6a (Supporting Information). After capacity decreases in the first 800 cycles, it increases from 5.4 mA h g^{-1} at 800th cycle to 51.1 mA h g^{-1} at 5200th cycle. Also, the charge–discharge curve (Figure S6b, Supporting Information) at 300th cycle shows a typical capacitance behavior, while the curve at 5200th cycle has evident discharge platform whose voltage is close to that of MnO_2 cathode material for ZIBs. The EDS result

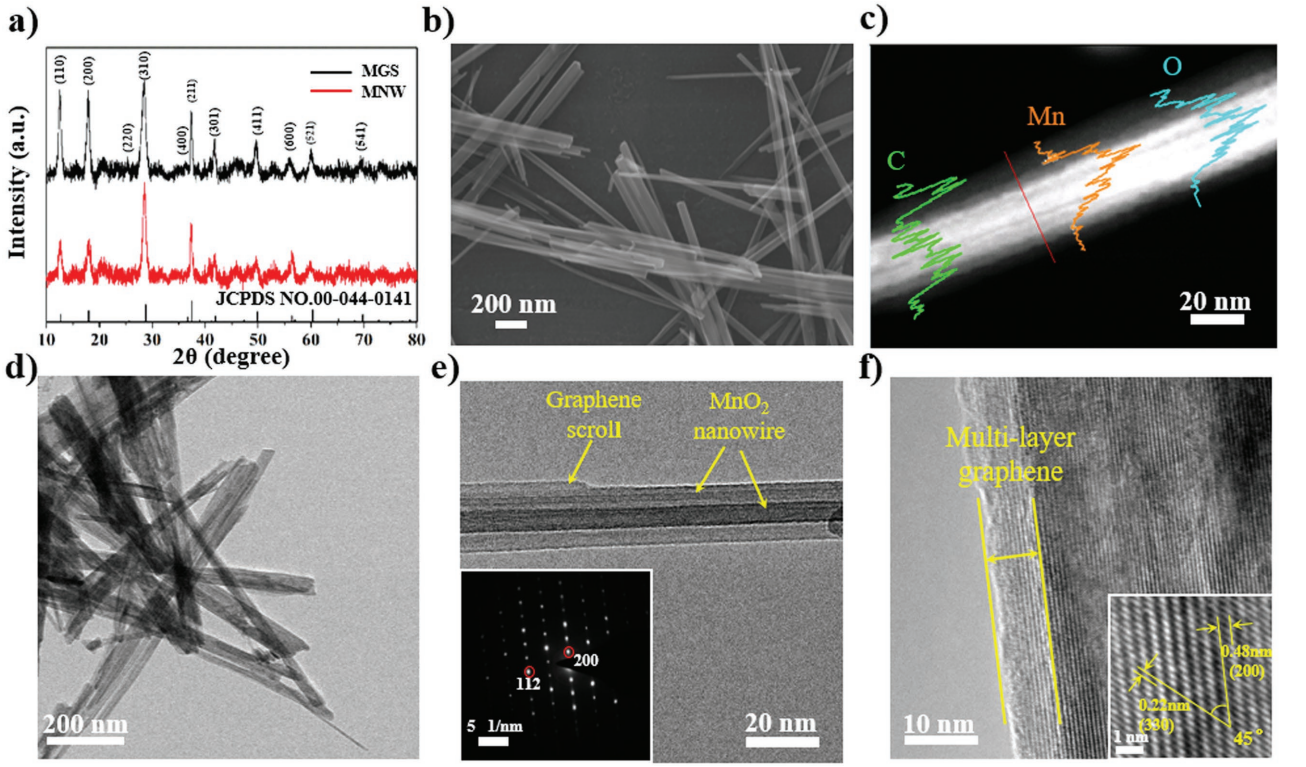

Figure 2. a) XRD patterns of MGS and MNW. b) SEM image of MGS. c) TEM image and corresponding EDS line scan result of MGS, showing the scanning route (red line), the element distributions of Mn (yellow line), C (green line), and O (cyan line), respectively. d,e) TEM images and SAED (inset in (e)) of MGS. f) The HRTEM of MGS.

of the rGO cathode after 5200 cycles is shown in Figure S6c (Supporting Information). A lot of Mn element deposits on rGO as the result of electrolyte decomposition. In addition to this, the TEM image of the MGS after 50 cycles in a 2 M $ZnSO_4$, 0.2 M $MnSO_4$ electrolyte under 1 A g^{-1} current density (Figure S6d, Supporting Information) was also provided to confirm the deposition of Mn^{2+}. We could found that after charging–discharging for 50 cycles, unlike the smooth surface shown in the Figure 2b,d, there are some small particles attached to the surface of the MnO_2 graphene scrolls (as yellow circles shows).

XPS, ex situ XRD, small angle X-ray diffraction (SAXD), in situ XRD, and GITT were applied to further explore the electrochemical mechanism of Zn/MGS battery. Figure S7a (Supporting Information) shows the XPS results of Zn 2p core level of insertion, extraction, and original states of MGS. The intensity of insertion state is higher than those of original and extraction states, which confirms the insertion/extraction of Zn^{2+} into MnO_2 framework.[19] Figure S7b–d (Supporting Information) show the 3s core level of initial, extraction, and insertion states of Mn element. The splitting of Mn 3s peak becomes wider when the valence of Mn in the oxide decreases because of fewer unpaired electrons in the 3d level.[17a,b,20] **Figure 4**a shows the ex situ XRD results of MGS collected at different discharge states (at the current density of 0.2 A g^{-1}). The results indicate that during the process of DP I, XRD pattern III (1.85 V), IV (1.40 V), and V (1.30 V) do not change obviously at 2θ range of 10°–80°. However, the SAXD (Figure 4c) results show a diffraction peak at 8.7°, the typical diffraction peak of (001) crystallographic plane of buserite. Buserite is suggested to have extra water layers along the center of MnO_2 tunnels with an interplanar spacing around 11 Å.[21] According to extended X-ray absorption fine structure performed by Chen group,[14b] the 2 × 2 MnO_6 octahedron breaks from the Mn–Mn corner to form the layer-type Zn-buserite with extra water layers. The water layers provide the channels for the insertion and extraction of Zn^{2+}. The intensity of the peak keeps increasing during DP I. However with more Zn^{2+} inserting into the MnO_2 framework during DP II, the structure of buserite becomes unstable, and then the peak shifts to 9.5° with full width at half-maximum increasing during the process of DP II, corresponding to the decrease of the interplanar spacing. During the process of DP II, as XRD patterns V (1.30 V), VI (1.20 V), and VII (1.00 V) show in Figure 4a, new peaks of tunnel-type $ZnMn_2O_4$ at 32.5° and 34.2° are observed. Figure 4b shows the detailed information of MNW and MGS at original and fully discharged states. The diffraction peaks at 32.5° and 34.5° of both MNW and MGS are observed, which means that rGO does not influence the intercalation mechanism of MnO_2. In situ XRD (Figure 4d) was also performed (at the current density of 0.2 A g^{-1}) to investigate the insertion/extraction mechanism of the cathode material in the 2θ range of 32.5°–34.5°. The peaks located at 32.5° and 34.2° in the first cycle only arise during the process of DP II, after the completion of DP I. From the GITT result (Figure 4e; Figure S8, Supporting Information), the diffusion coefficient (D) of MGS can be obtained via the following equation[22]

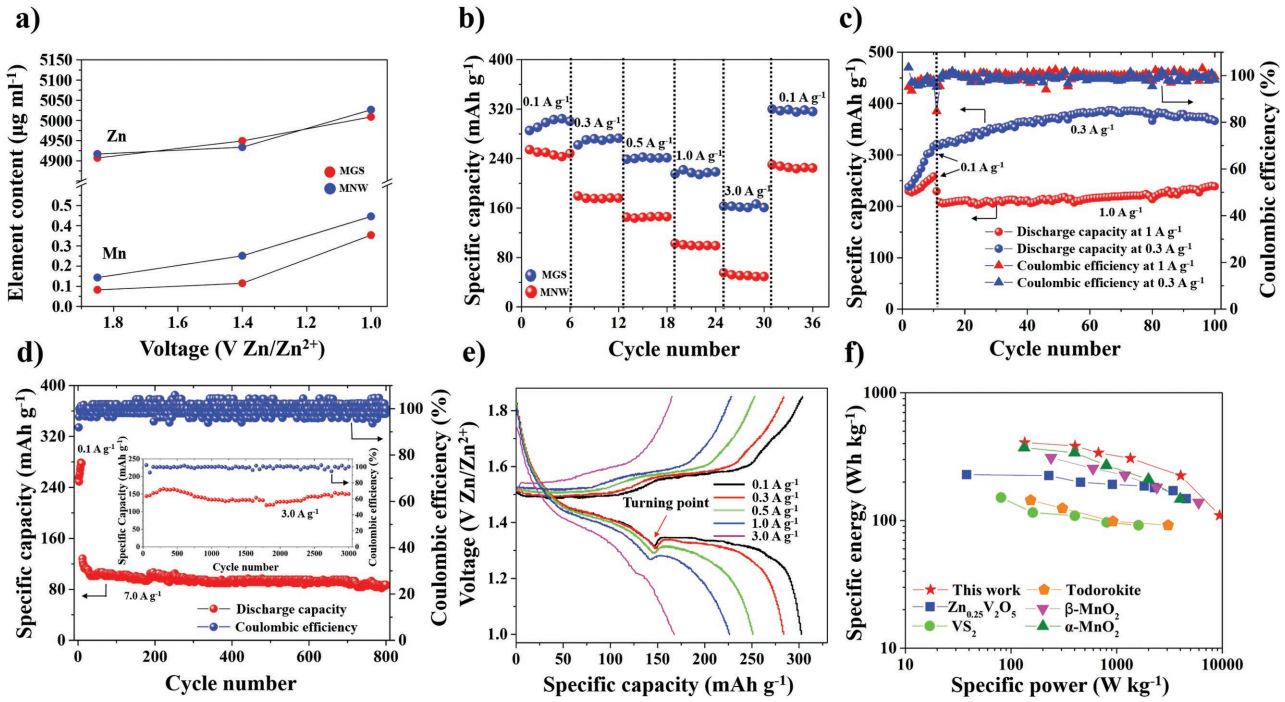

Figure 3. The electrochemical performance of MGS and MNW. a) Element analysis of Zn^{2+} and dissolved Mn^{2+} in a 2 M $ZnSO_4$ aqueous electrolyte during the discharge process of first cycle tested in a two-electrode system. b) Rate performances of MGS and MNW. c) Cycling performances of MGS at 0.3 and 1 A g^{-1} after an activation process at 0.1 A g^{-1}. d) Long-term cycling performances at 7 and 3 A g^{-1} (inset). e) Charge and discharge curves of MGS at current densities ranging from 0.1 to 3 A g^{-1}. f) Comparison of the Ragone plot (based on the weight of cathode material) of the MGS cell with some other known cathode materials for aqueous ZIBs.

$$D = \frac{4}{\pi t}\left(\frac{m_B V_M}{M_B S}\right)^2\left(\frac{\Delta E_S}{\Delta E_\tau}\right)^2 \quad (1)$$

where τ is the constant current pulse time, m_B, V_M, S, and M_B are the mass, molar volume, electrode–electrolyte interface area, and molar mass of MnO_2, respectively. Based on the GITT result, the two-step intercalation reactions in MGS cathode and Zn anode can be summarized as below

In cathode

During DP I

$$2xe^- + MnO_2 + xZn^{2+} \leftrightarrow Zn_xMnO_2\ (0 < x < 0.27) \quad (2)$$

During DP II

$$2(x-0.27)e^- + Zn_{0.27}MnO_2 + (x-0.27)Zn^{2+} \leftrightarrow Zn_xMnO_2\ (0.27 < x < 0.59) \quad (3)$$

In anode

$$Zn - 2e^- \leftrightarrow Zn^{2+} \quad (4)$$

From the calculated results, the diffusion coefficient in DP I is much lager than that of DP II, referring that the insertion speed of Zn ions in DP I is faster than that of DP II. Therefore, when the voltage drops to the turning point around 1.30 V, the sudden change of the insertion speed causes the temporary accumulation of the reactant. This is reflected in the charge–discharge curve (Figure 3e; Figure S5a, Supporting Information) in which the turning point locates at around 1.30 V, and the voltage first decreases, then increases and finally decreases. We attribute this sudden change of the insertion speed to different Zn-insertion sites. As Figure 4f shows, in the process of DP I, Zn ions first insert into the water layers mentioned above to form Zn-buserite, until no more Zn ions can be held (process of DP I). Then Zn ions deeply insert into the 2 × 2 tunnels of α-MnO_2 (process of DP II). The volume change and electrostatic interaction in DP II are more violent than those in DP I, which may cause irreversible destruction of the crystal structure of MnO_2 and slow down the insertion speed of Zn ions. These differences are also reflected in the rate performances of MGS and MNW (Figure 3b; Figure S5a,b, Supporting Information), in which both capacities of DP II of MGS and MNW decrease faster than those of DP I. The rate capacity is greatly improved after coating of rGO on the MNW, which can stabilize the structure and improve the electrical conductivity of MnO_2 as the cathode material for aqueous ZIB. Besides, rGO can also provide extra adsorption sites for Zn ions, enhancing the adsorption ability of the cathode material.

3. Conclusion

In summary, aqueous Zn/MGS battery is designed and constructed in this work. The rGO reduces the dissolution of cathode material and greatly improves the electrical conductivity

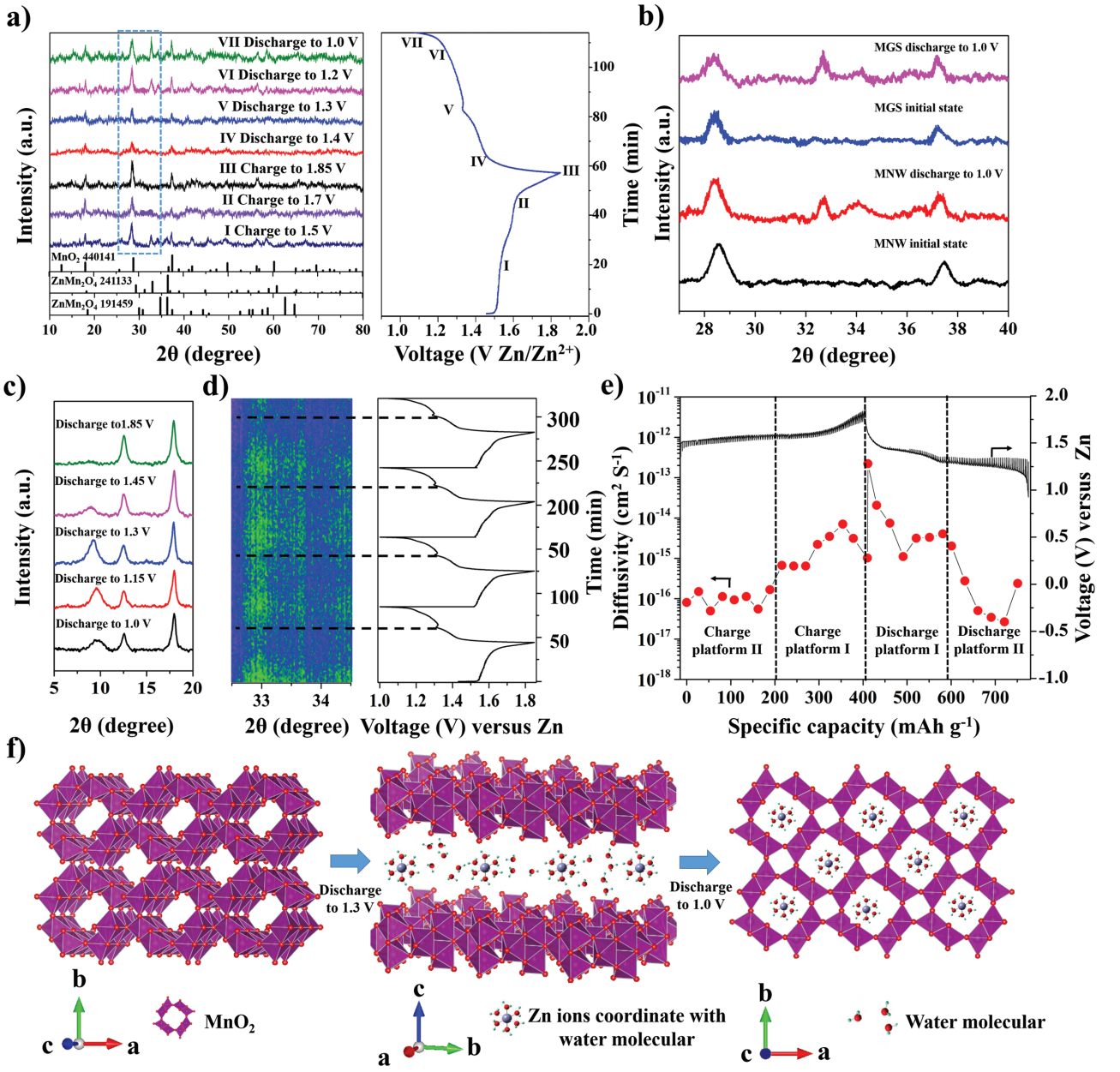

Figure 4. a) Ex situ XRD patterns of MGS collected at various states. b) XRD patterns of MNW and MGS at the initial state and discharge state. c) SAXD pattern of MGS in 2 θ range of 5°–20° collected at various states. d) In situ XRD pattern with 2 θ range of 32.5°–34.5°. e) GITT curve and diffusivity versus state of charge and discharge. f) Schematic illustration of the two-step intercalation mechanism of MGS cathode.

and capacity of MnO_2 as the cathode material for aqueous ZIB, delivering a high capacity of 362.2 mA h g^{-1} (406.6 Wh kg^{-1}) at the current density of 0.3 A g^{-1} after 100 cycles. Besides, the battery also exhibits considerable long-term cycling stability (a specific capacity of 145.3 mA h g^{-1} is attained at 3 A g^{-1}, with high retention of 94% after 3000 cycles) and good rate performance compared with bare MNW. In addition, a two-step intercalation mechanism that Zn ions first insert into the layers and then the tunnels of MnO_2 framework, is elucidated and proved by in situ XRD, GITT, and XPS characterizations. We believe the graphene scroll-coated α-MNW cathode will bring intensive interests and great potential for aqueous ZIB.

4. Experimental Section

Synthesis of MNW and MGS: In a typical synthesis of pure MNW, 3 mmol $MnSO_4 \cdot H_2O$ and 2 mL 0.5 mol L^{-1} H_2SO_4 were dissolved in 60 mL DI water and stirred for 10 min. Then, 20 mL 0.1 mol L^{-1} $KMnO_4$ was dropwise added to the solution. Afterward, the mixture

was vigorously stirred at room temperature for 1 h, followed by ultrasonication for 30 min before the mixture was sealed into a 100 mL Teflon-lined autoclave for 12 h at 120 °C. Finally, the obtained product was collected by centrifugation after cooling, and washed with DI water for three times, then dried using a freezing dryer. MGS-0.9%, 1.8%, 2.7%, and 3.6% employed the same procedure described above, with the addition of 1, 2, 3, and 4 mL 2 mg mL^{-1} rGO dispersion by a Hummer's method after the $KMnO_4$ was added, respectively.

Material Characterizations: The prepared samples were characterized by powder X-ray diffraction (XRD, D8 Discover X-ray diffractometer with Cu Kα radiation, λ = 1.5406 Å). The SAXD test was performed on Rifagu MiniFlex 600. The structures and morphologies were characterized by transmission electron microscope (TEM, JEOL JEM-2100F STEM/EDS microscope) and field-emission scanning electron microscopy (FESEM, JSM-7100F). The element contents were determined by inductively coupled plasma-atomic emission spectroscopy (ICP-AES) on a PLASMA 300 apparatus, and its accuracy is 0.1%. EDS measurement was performed using an Oxford EDS IE250. XPS characterization was conducted on Thermo Scientific Escalab 250Xi. Raman spectra were obtained using a Renishaw INVIA. TG analysis was conducted on a Netzsch STA449F3 simultaneous thermal analyzer to explore the carbon content in samples.

In situ XRD experiments during an electrochemical test of batteries were performed on a D8 Discover X-ray diffractometer equipped with a nonmonochromated Cu Kα X-ray source. The samples were scanned over the 2θ ranging from 25° to 45°.

Electrochemical Characterizations: The MNW and MGS electrodes were prepared by mixing MNW or MGS (70 wt%), acetylene black (Super-P, 20 wt%), and polytetrafluoroethylene (10 wt%). Then the ground slurry was tableted and cut into Φ10 mm electrodes. Zinc foil and glass fiber membrane were used as the anode and separator, respectively, and 2 M zinc sulfate with 0.2 M manganese sulfate additive solution was employed as the electrolyte. A CR2016-type coin cell was assembled in air to evaluate the electrochemical performance with a LAND battery testing system (CT2001A). CVs, electrochemical impedance spectroscopy, and galvanostatic intermittent titration technique result were measured on a CHI760E electrochemical workstation.

Supporting Information

Supporting Information is available from the Wiley Online Library or from the author.

Acknowledgements

This work was supported by the National Natural Science Fund for Distinguished Young Scholars (51425204), the National Natural Science Foundation of China (51502227, 51579198), the National Key Research and Development Program of China (Grant Nos., 2016YFA0202603 and 2016YFA0202604), the Programme of Introducing Talents of Discipline to Universities (Grant No. B17034), the China Postdoctoral Science Foundation (Grant No. 2015T80845), the project of Innovative group for low cost and long cycle life Na ion batteries R&D and industrialization of Guangdong Province (Grant No. 2014ZT05N013), the Hubei Province Natural Science Fund (2016CFB582), Wuhan Morning Light Plan of Youth Science and Technology (Grant No. 2017050304010316), the State Key Laboratory of Advanced Technology for Materials and Processing at Wuhan University of Technology (2016-KF-1), the Key Laboratory of Functional Inorganic Material Chemistry (Heilongjiang University), Ministry of Education. We thank Prof. Xiangfeng Duan of University of California, Los Angeles, for strong support and stimulating discussions, and the Fundamental Research Funds for the Central Universities (WUT: 2016III005, 2017III009, 2017III005, and 2017III030). M.Y. acknowledges the financial support from the State of Washington through the University of Washington Clean Energy Institute.

Conflict of Interest

The authors declare no conflict of interest.

Keywords

cathode materials, graphene scroll-coated α-MnO_2, high performance, Zn-ion batteries

Received: November 5, 2017
Revised: December 11, 2017
Published online:

[1] a) Y. Idota, T. Kubota, A. Matsufuji, Y. Maekawa, T. Miyasaka, *Science* **1997**, *276*, 1395; b) P. Poizot, S. Laruelle, S. Grugeon, L. Dupont, J. M. Tarascon, *Nature* **2000**, *407*, 496; c) L. Q. Mai, X. C. Tian, X. Xu, L. Chang, L. Xu, *Chem. Rev.* **2014**, *114*, 11828; d) Y. G. Guo, J. S. Hu, L. J. Wan, *Adv. Mater.* **2008**, *20*, 2878; e) E. Yoo, J. Kim, E. Hosono, H. S. Zhou, T. Kudo, I. Honma, *Nano. Lett.* **2008**, *8*, 2277.

[2] a) J. M. Tarascon, M. Armand, *Nature* **2001**, *414*, 359; b) J. B. Goodenough, Y. Kim, *Chem. Mater.* **2010**, *22*, 587; c) P. G. Bruce, S. A. Freunberger, L. J. Hardwick, J. M. Tarascon, *Nat. Mater.* **2012**, *11*, 19; d) B. Wang, Y. Wang, B. Sun, P. Munroe, G. Wang, *RSC Adv.* **2013**, *3*, 5069; e) M. S. Whittingham, *Chem. Rev.* **2004**, *104*, 4271.

[3] a) C. J. Xu, B. H. Li, H. D. Du, F. Y. Kang, *Angew. Chem.* **2012**, *51*, 933; b) M. H. Alfaruqi, V. Mathew, J. Gim, S. Kim, J. J. Song, J. P. Baboo, S. H. Choi, J. Kim, *Chem. Mater.* **2015**, *27*, 3609.

[4] M. Hilder, B. Winther-Jensen, N. B. Clark, *Electrochim. Acta* **2012**, *69*, 308.

[5] Z. Liu, G. Pulletikurthi, F. Endres, *ACS Appl. Mater. Interfaces* **2016**, *8*, 12158.

[6] P. Senguttuvan, S. D. Han, S. Kim, A. L. Lipson, S. Tepavcevic, T. T. Fister, I. D. Bloom, A. K. Burrell, C. S. Johnson, *Adv. Energy Mater.* **2016**, *6*, 1600826.

[7] D. Kundu, B. D. Adams, V. Duffort, S. H. Vajargah, L. F. Nazar, *Nat. Energy* **2016**, *1*, 16119.

[8] P. He, M. Yan, G. Zhang, R. Sun, L. Chen, Q. An, L. Mai, *Adv. Energy Mater.* **2017**, *7*, 1601920.

[9] a) Y. Shen, K. Kordesch, *J. Power Sources* **2000**, *87*, 162; b) C. C. Yang, S. J. Lin, *J. Power Sources* **2002**, *112*, 174.

[10] a) M. H. Alfaruqi, J. Gim, S. Kim, J. J. Song, J. Jo, S. Kim, V. Mathew, J. Kim, *J. Power Sources* **2015**, *288*, 320; b) N. Tang, X. K. Tian, C. Yang, Z. B. Pi, Q. Han, *J. Phys. Chem. Solids* **2010**, *71*, 258; c) D. Aurbach, Z. Lu, A. Schechter, Y. Gofer, H. Gizbar, R. Turgeman, Y. Cohen, M. Moshkovich, L. Mikhael, *Nature* **2000**, *407*, 724.

[11] H. L. Pan, Y. Y. Shao, P. F. Yan, Y. W. Cheng, K. S. Han, Z. M. Nie, C. M. Wang, J. H. Yang, X. L. Li, P. Bhattacharya, K. T. Mueller, J. Liu, *Nat. Energy* **2016**, *1*, 16039.

[12] a) Y. Zeng, X. Zhang, Y. Meng, M. Yu, J. Yi, Y. Wu, X. Lu, Y. Tong, *Adv. Mater.* **2017**, *26*, 1700214; b) P. Hu, M. Y. Yan, X. P. Wang, C. H. Han, L. He, X. J. Wei, C. J. Niu, K. N. Zhao, X. C. Tian, Q. L. Wei, Z. J. Li, L. Q. Mai, *Nano Lett.* **2016**, *16*, 1523; c) S. Chen, J. Zhu, X. Wu, Q. Han, X. Wang, *ACS Nano* **2010**, *4*, 2822; d) K. Xu, *Chem. Rev.* **2014**, *114*, 11503; e) M. Y. Yan, F. C. Wang, C. H. Han,

X. Y. Ma, X. Xu, Q. Y. An, L. Xu, C. J. Niu, Y. L. Zhao, X. C. Tian, P. Hu, H. G. Wu, L. Q. Mai, *J. Am. Chem. Soc.* **2013**, *135*, 18176.

[13] D. W. Xu, B. H. Li, C. G. Wei, Y. B. He, H. D. Du, X. D. Chu, X. Y. Qin, Q. H. Yang, F. Y. Kang, *Electrochim. Acta* **2014**, *133*, 254.

[14] a) B. Lee, H. R. Lee, H. Kim, K. Y. Chung, B. W. Cho, S. H. Oh, *Chem. Commun.* **2015**, *51*, 9265; b) N. Zhang, F. Cheng, J. Liu, L. Wang, X. Long, X. Liu, F. Li, J. Chen, *Nat. Commun.* **2017**, *8*, 1.

[15] A. Bello, O. O. Fashedemi, M. Fabiame, J. N. Lekitima, K. I. Ozoemena, N. Manyala, *Electrochim. Acta* **2013**, *3*, 1094.

[16] a) K. F. Chen, S. Y. Song, D. F. Xue, *J. Mater. Chem. A* **2015**, *3*, 2441; b) K. F. Chen, Y. D. Noh, K. Y. Li, S. Komarneni, D. F. Xue, *J. Mater. Chem. C* **2013**, *117*, 10770; c) K. F. Chen, W. Pan, D. F. Xue, *J. Mater. Chem. C* **2016**, *120*, 20077.

[17] a) D. Gosztola, M. J. Weaver, *ChemInform* **1990**, *21*, 141; b) E. Widjaja, J. T. Sampanthar, *Anal. Chim. Acta* **2007**, *585*, 241.

[18] J. Lee, J. B. Ju, W. L. Cho, B. W. Cho, S. H. Oh, *Electrochim. Acta* **2013**, *112*, 138.

[19] N. Zhang, F. Y. Cheng, Y. C. Liu, Q. Zhao, K. X. Lei, C. C. Chen, X. S. Liu, J. Chen, *J. Am. Chem. Soc.* **2016**, *138*, 12894.

[20] a) D. Gosztola, M. J. Weaver, *ChemInform* **1990**, *21*, 141; b) E. Widjaja, J. T. Sampanthar, *Anal. Chim. Acta* **2007**, *585*, 241; c) M. Chigane, M. Ishikawa, M. Izaki, *J. Electrochem. Soc.* **2001**, *148*, D96.

[21] a) S. Goldberg, R. A. Glaubig, *Clays Clay Miner.* **1987**, *35*, 220; b) A. Manceau, E. Silvester, C. Bartoli, B. Lanson, V. A. Drits, *Am. Mineral.* **1997**, *82*, 1150.

[22] E. Deiss, *Electrochim. Acta* **2005**, *50*, 2927.